width enhancement using a reactive impedance substrate, IEEE Trans Antennas Propagat 52 (2004), 2403–2414.

13. Y. Zhao, Y. Hao, and C.G. Parini, Radiation properties of PIFA on electromagnetic bandgap substrates, Microwave Opt Technol Lett 44 (2005), 21–24.

14. M.V. Kostin and V.V. Shevchenko, Artificial magnetics based on double circular elements, Proc Bianisotropics'94, Périgueux, France, 1994, pp. 49–56.

15. P. Ikonen, S.I. Maslovski, I.A. Kolmakov, and S.A. Tretyakov, New artificial high permeability material for microwave applications, Progress Electromagn Res Symp, Pisa, Italy, 2004, pp. 485–488.

16. K. Buell, H. Mosallaei, and K. Sarabandi, Embedded-circuit magnetic metamaterial substrate performance for patch antennas, IEEE Antennas Propagat Soc Int Symp, Monterey, CA, 2004, pp. 1415–1418.

17. M.K. Kärkkäinen, S.A. Tretyakov, and P. Ikonen, Numerical study of a PIFA with dispersive material fillings, Microwave Opt Technol Lett 45 (2005), 5–8.

18. L.L. Rauth, J.S. McLean, K.R. Dorner, J.R. Casey, and G.E. Crook, Broadband, low-profile antenna for portable data terminal, IEEE Antennas Propagat Soc Int Symp, Montreal, Canada, 1997, pp. 438–441.

19. F.-R. Hsiao and K.-L. Wong, Compact planar inverted-F patch antenna for triple-frequency operation, Microwave Opt Technol Lett 33 (2002), 459–462.

20. K.L. Virga and Y. Rahmat-Samii, Low-profile enhanced-bandwidth PIFA antennas for wireless communications packaging, IEEE Trans Microwave Theory Tech 45 (1997), 1879–1888.

21. P. Salonen, M. Keskilammi, and M. Kivikoski, Single-feed dual-band planar inverted-F antenna with U-shaped slot, IEEE Trans Antennas Propagat 48 (2000), 1262–1264.

22. D.M. Pozar, Microstrip antennas, Proc IEEE 80 (1992), 79–91.

23. H.A. Wheeler, Fundamental limitations of small antennas, Proc IRE 35 (1947), 1479–1484.

24. R.C. Hansen, Fundamental limitations in antennas, Proc IEEE 69 (1981), 170–182.

25. T. Taga and K. Tsunekawa, Performance analysis of a built-in planar inverted-F antenna for 800-MHz band portable radio units, IEEE J Sel Areas Commun 5 (1987), 921–929.

26. P. Vainikainen, J. Ollikainen, O. Kivekäs, and I. Kelander, Resonator-based analysis of the combination of mobile handset antenna and chassis, IEEE Trans Antennas Propagat 50 (2002), 1433–1444.

27. J. Villanen, J. Ollikainen, O. Kivekäs, and P. Vainikainen, Compact antenna structures for mobile handsets, Proc IEEE 58th Vehic Technol Conf, Orlando, FL, 2003, pp. 40–44.

28. S. Tretyakov, Analytical modelling in applied electromagnetics, Artech House, Norwood, MA, 2003.

STEADY-STATE ANALYSIS OF A DIRECTIONAL SQUARE LATTICE BAND-EDGE PHOTONIC CRYSTAL LASERS

Rogério M. Cazo,[1] Carmem L. Barbosa,[1] Haroldo T. Hattori,[2] and Vitor M. Schneider[3]
[1] Photonics Division
Instituto de Estudos Avançados-CTA
São José dos Campos SP, Brazil
[2] LEOM-CNRS-Ecole Centrale de Lyon
36 Avenue de Collongue
69134 Ecully, France
[3] 19 Eagle Drive, Apt. 202
Painted Post, NY 14870

ABSTRACT: *The original square-lattice band-edge structure emitted light in different directions. In a recent paper [18], we have improved the directivity of these structures by using a honeycomb photonic crystal to shield the original structure. This has improved the performance of such devices, in such a way that light can be coupled directionally to a large waveguide. In this paper, we present a steady-state analysis of the performance of this directive device and study the amount of power which can be coupled into the waveguide, analyzing its performance as an in-plane emitter and the limitations caused by vertical losses.* © 2005 Wiley Periodicals, Inc. Microwave Opt Technol Lett 46: 210–214, 2005; Published online in Wiley InterScience (www.interscience.wiley.com). DOI 10.1002/mop.20947

1. INTRODUCTION

Photonic crystals (PhCs) are periodic structures of high index contrast, which present the property of forbidding the propagation of light in a certain wavelength range, a property that can be used to manipulate the flow of light in different ways. A complete photonic bandgap for all directions and polarizations can be obtained using 3D PhCs, but their fabrication processes are not very well controlled and they tend to have many imperfections. On the other hand, fabrication of bidimensional (2D) PhCs has been well established and a multitude of devices have already been produced, such as filters [1–3], waveguide bends and branches [4, 5], lasers [6–18], and so forth.

One possible major contribution of PhCs will be in the area of compact and efficient laser devices. PhCs allow the confinement of light in small volumes, which can change their optical-emission properties, thus allowing both enhancement and inhibition [15]. The most common configurations for these devices are defect-mode [6–9], surface-emitting [10–12], and band-edge [13–14, 16–18] lasers. Defect-mode lasers can have quality factors (Q) as high as 10,000 and low threshold currents, but as argued by Ohnishi et al. [12], broad-area lasers such as band-edge lasers have the advantage of providing larger output power, better heat dissipation, and narrower beam-divergence.

Band-edge lasers operate at the edges of the first Brillouin zone, at high-symmetry points (for example, the X point in a square lattice of air holes). In many cases, the high-symmetry points of a given mode present extreme points in their band diagrams. At these extreme points, the group velocity of a given mode can be made very small, that is, the average lifetime of the photons in the active area can be made large, thus significantly reducing the size of the device [13]. Band-edge lasers can be considered as the photonic-crystal equivalents to DFB lasers. Actually, band-edge lasers in triangular [13] and square [14] lattices of air holes have been analyzed recently. However, thus far these devices have emitted light in different directions.

Our band-edge laser will have a main PhC that consists of square lattices of air holes in a semiconductor slab and will operate at the X point in the first Brillouin zone. Without loss of generality, we will restrict our attention to the transverse electric (TE) modes (using the same convention as in [4]), and the operating mode will be the first one in the valence band. Initially, we describe the original and modified structures and, subsequently we shall present a steady-state analysis of the directive laser device, including the effects of vertical losses. These effects were also commented upon in a recent paper by Topol'ancik et al. [17], in which laser sources with defect-cavities coupled light to W1 waveguides. In this recent paper, it was shown that the coupling of light to narrow waveguides was severely degraded by vertical losses (a fact that explained why the coupled power into a W1 waveguide was in the range of tens of pW).
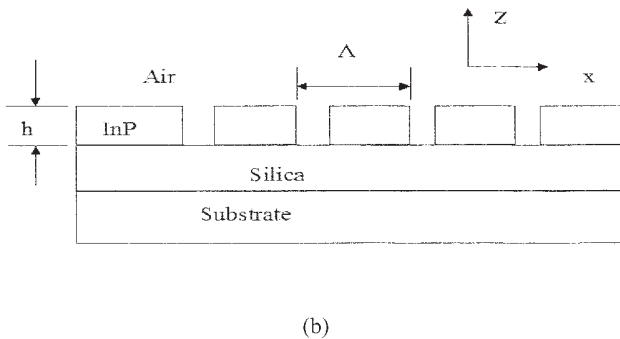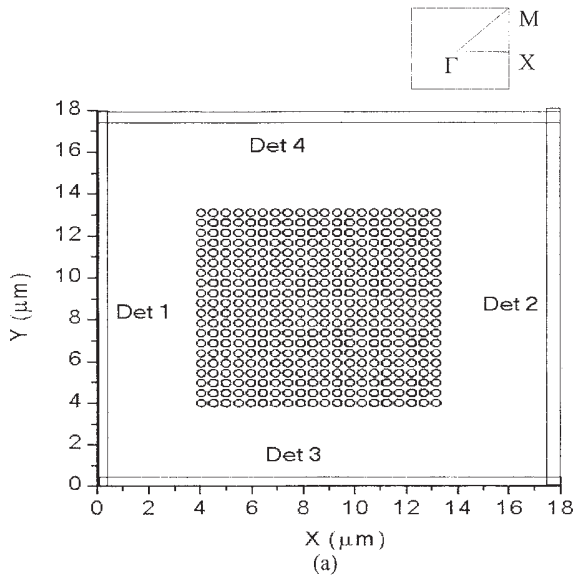
Figure 1 (a) General view of an ordinary square-lattice DFB laser in the x–y plane (the air holes are assumed to be etched in the InP layer); (b) Y-cut of the device, showing its different layers

2. ANALYSIS OF DIRECTIVE STRUCTURES

The basic band-edge structure is illustrated in Figure 1(a). It consists of a square lattice of air holes fabricated in an InP layer of thickness $h = 250$ nm. Above and below this InP layer, there are air and silica layers. The silica layer is thick enough so that the amount of light that reaches the substrate (InP, for example) is negligible in comparison with the field in the PhC layer [see Fig. 1(b)]. The filling factor (ff) of the main photonic crystal (the volume occupied by the air holes in a primitive cell divided by the volume of the primitive cell) is assumed to be 40%. Its band diagram along the ΓX direction is shown in Figure 2(a). This device shall operate at the X point of mode 1, at the edge of the first Brillouin zone, as shown in Figure 2(a). In order to operate close to $\lambda = 1550$ nm (with λ the free-space wavelength), the lattice constant is chosen to be $\Lambda = 480$ nm, and the radius of the air holes $r = 170$ nm. This band diagram is calculated using MIT's photonic-band software [19], with the normalized frequency expressed in units of Λ/λ and the normalized wave vector in units of $2\pi/\Lambda$ (the wave vector at the X point, for the first Brillouin zone, is equal to π/Λ).

In order to provide sufficient data for a steady-state analysis of this laser device, we perform 3D finite-difference time-domain (FDTD) calculations. Absorbing layers are placed at the boundaries of the computation area. The temporal-envelope function of the source is either a pulse (used to obtain the spectra for different

structures) or constant (continuous-wave excitation). The source is oriented in the y-direction and is generally a Gaussian beam located in a region of maximum electric field. Power detectors are placed along four directions in the InP layer ("rectangles" located at x, y = constant and covering a lateral region of this layer) outside the PhC region: the first one is close to the border $x = 0$ of the computation area (detector 1), the second one is close to the end of the wide waveguide ($x = 18$ μm) (detector 2), the third one is close to $y = 0$ (detector 3), and the last one is close to $y = 18$ μm (detector 4). As we have provided the details concerning our FDTD simulations, from here on we shall refer to the FDTD data as simply 3D-FDTD field distribution (and also generally refer to H_z), and so forth. More details about these simulations are found in [11, 18].

The basic PhC has a power reflectivity of about 96% (field reflectivity, $|r_{eff}|$, of about 0.980) at $\lambda = 1502$ nm. About 70% of this reflected power remains in the core of the waveguide (InP layer), while the rest is either in the cladding regions (air and silica regions) or scattered away from the waveguide. The group velocity along the ΓX direction is about 3.06×10^6 m/s. Based upon the FDTD simulations, we can estimate that 12% of the incident power is lost in the silica region and 5% in the air region.

For the original structure [Fig. 1(a)], the main resonant peak at the X point appears at $\lambda = 1502.1$ nm, with a Q of about 700.
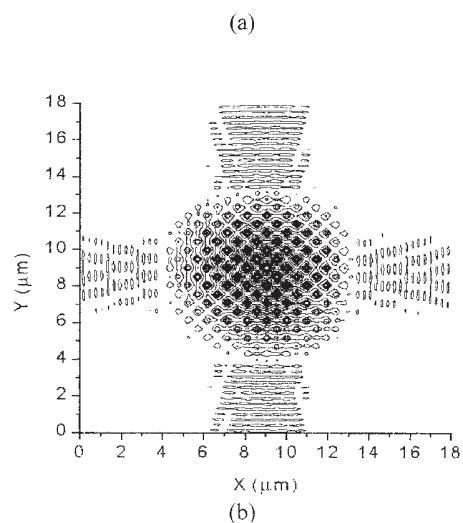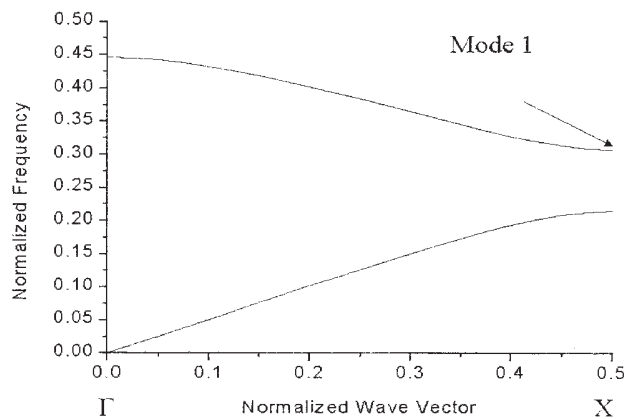

Figure 2 (a) Band diagram for the square lattice of air holes along the ΓX direction; (b) field distribution H_z in the x–y-plane for this basic structure at the X-point resonance
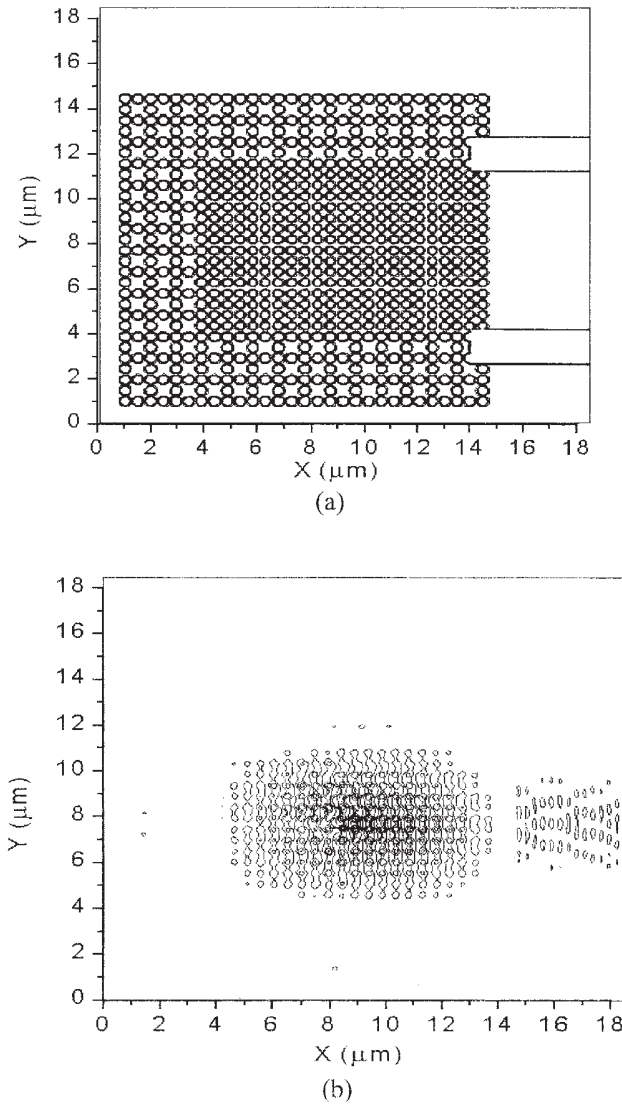
Figure 3 (a) Square lattice "shielded" by a square honeycomb lattice of air holes; (b) 3D-FDTD field distribution H_z at $\lambda = 1504.4$ nm in the x–y plane

Figure 2(b) shows the field distribution for this structure at resonance. As it can be observed from this figure, the device emits in different directions—in our case, along four directions. In order to improve the directionality of this basic structure, we have shielded three sides of this structure with a honeycomb structure operating at its bandgap, as illustrated in Figure 3(a). The radius of the holes for the honeycomb structure is chosen as $r = 200$ nm, while the radius of the holes in the basic square lattice remains $r = 170$ nm. The main peak for this modified structure appears at $\lambda = 1504.4$ nm, with $Q = 1000$. Other peaks occur at $\lambda = 1514$ nm, 1530 nm, and so on. As can be observed in Figure 3(b), the field exits mainly along the $+x$-direction and is inserted in a waveguide. The FDTD calculations show that about 1.3% of the incident power is inserted in the waveguide, as expected, given that the transmission in the waveguide should be less than $1 - |r_{eff}|^2$.

3. STEADY-STATE ANALYSIS OF THE LASER DEVICE

In order to have a preliminary calculation of the performance of this device as a laser, we have used a type of classical model for the device. Although there are other methods used in the analysis of laser action, such as those found in [16, 20], this approach provides a first estimate of the performance of the device and is easily understandable. We will restrict the attention to the device with a honeycomb shielding and the only possible in-plane escape (in the InP layer) is through the waveguide.

Based on previous FDTD simulations, it is possible to calculate r_{eff} as described in the previous section. Once we have determined the field reflectivities at the interface between the PhC and the waveguide, we can calculate the mirror losses as (assuming that the reflectivities at the other sides are 1) as follows:

$$\alpha_m = 1/L \ \ln(1/|r_{eff}|), \tag{1}$$

where L is the total length of the cavity (here assumed to be about 10 μm). In this case, we find $\alpha_m = 2041.1$ m^{-1}. The vertical losses are included as

$$\alpha_{vert} = \frac{1}{2L} \ln\left[\frac{1}{1 - P_{vert}}\right], \tag{2}$$

where P_{vert} is the percentage of power that is lost in the vertical direction for each roundabout of photons in the PhC cavity. Initially, we assume that $P_{vert} = 0.17$, providing $\alpha_{vert} = 9316.48$ m^{-1}. Considering the internal losses (α_{int}) as 3000 m^{-1}, we find that the total losses can be expressed as

$$\alpha_{total} = \alpha_{vert} + \alpha_m + \alpha_{int} = 14357.58 \text{ m}^{-1}. \tag{3}$$

Considering a laser with four quantum wells of In$_{0.53}$Ga$_{0.47}$As (Q 1.25) with 7 nm of width (t_w, same as used in [21]), its power gain g is given by

$$g = 5.83 \times 10^4 \ln(J/8.1 \times 10^5) \text{ m}^{-1}, \tag{4}$$

where J is the density of current in the active region. The threshold condition can be expressed as [21]:

$$\Gamma_{xy} g \xi_m n_w t_w / t_{InP} = \alpha_{total}, \tag{5}$$

where Γ_{xy} is the lateral confinement factor (about 0.8), ξ_m is the gain-enhancement factor of the resonant mode in the PhC (about 1.65 for the chosen mode [16, 18]), n_w is the number of quantum wells, and t_{InP} is the thickness of the InP layer.

Based on these values, the threshold current density is about 4.285×10^6 A/m^2. Assuming that the current cannot pass through the air holes and that the current passes through an area of 100 μm^2, the threshold current is given by

$$I_{th} = J_{th} \times 10^{-10}(1 - \pi(0.17/0.48)^2) = 260 \ \mu\text{A}. \tag{6}$$

The power that is coupled through the waveguide is given by [21]:

$$P_{cw} = \frac{\eta_i \eta_a \alpha_m hc}{\lambda q \alpha_{total}} (I - I_{th}) = \eta_d \frac{hc}{\lambda q} (I - I_{th})$$
$$= 0.03055(I - 2.6 \times 10^{-4}) \text{ W}, \tag{7}$$

where η_i is the terminal-current fraction providing carriers that recombine in the active region (here assumed to be around 0.8), $\eta_a = 1.3/4 = 0.325$ denotes the "extra" coupling losses (remember that FDTD simulations have provided a transmission smaller
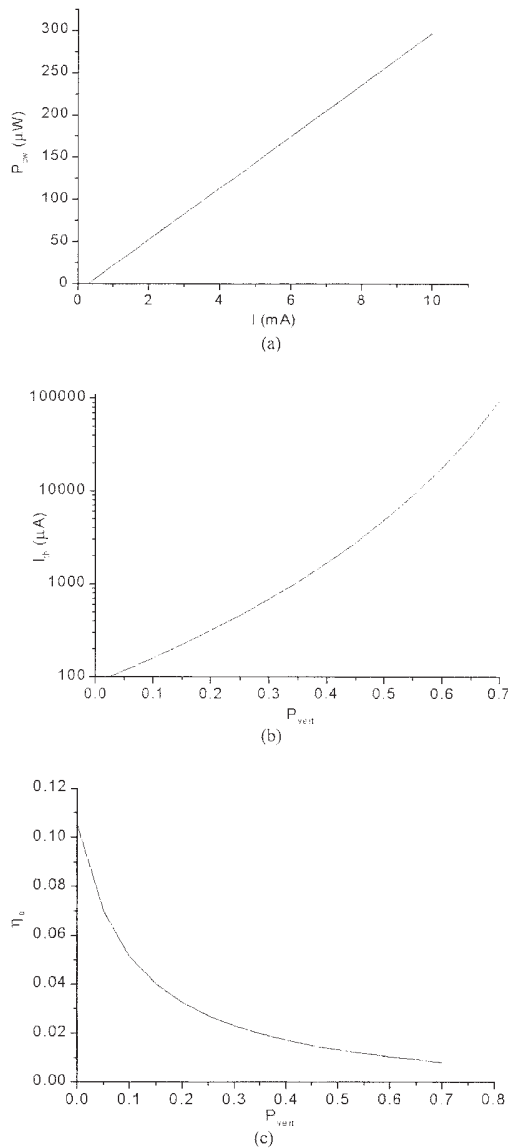
Figure 4 (a) Power coupled to the waveguide (in μW) as a function of the injection current (mA) for $P_{vert} = 0.17$; (b) threshold current as a function of P_{vert}; (c) differential quantum efficiency as a function of P_{vert}

CONCLUSION

A scheme to provide directionality to band-edge laser structures has been presented. For this chosen directive structure, a steady-state analysis was performed to study the performance of this device. From this study, we can expect that this device can couple light in a wide waveguide in the range of tens of μW. At the same time, we may state that the vertical losses will deeply influence the performance of these devices, even when the "lasing" of these devices is avoided. This analysis has shown that this device should support up to 50% of vertical losses before sensibly degrading its performance.

REFERENCES

1. S. Fan, P.R. Villeneuve, and J.D. Joannopoulos, Channel drop filters in photonic crystals, Optics Express 3 (1998), 4–11.
2. T. Asano, M. Mochizuki, S. Noda, M. Okano, and M. Imada, A channel drop filter using a single defect in a 2D photonic crystal slab: Defect engineering with respect to polarization mode and ratio of emissions from upper and lower sides, J Lightwave Technol 21 (2003), 1370–1376.
3. T. Matsumoto and T. Baba, Photonic crystal k-vector superprism, IEEE/OSA J Lightwave Technol 22 (2004), 917–922.
4. S. Fan, S.G. Johnson, J.D. Joannopoulos, C. Manolatou, and H.A. Haus, Waveguide branches in photonic crystals, J Optics Soc Am B 18 (2001), 162–165.
5. J. Smajic, C. Hafner, and D. Erni, Design and optimization of an achromatic photonic crystal bend, Optics Express 11 (2003), 1378–1384.
6. O. Painter, R.K. Lee, A. Scherer, A. Yariv, J.D. O'Brien, P.D. Dapkus, and I. Kim, Two-dimensional photonic band-gap defect mode laser, Sci 284 (1999), 1819–1821.
7. P.T. Lee, J.R. Cao, S.J. Choi, Z.J. Wei, and J.D. O'Brien, Operation of photonic crystal membrane lasers above room temperature, Appl Phys Lett 81 (2002), 3311–3313.
8. H.G. Park, J.K. Hwang, J. Huh, H.Y. Ryu, S.H. Kim, J.S. Kim, and Y.H. Lee, Characteristic of modified single-defect two-dimensional photonic crystal lasers, IEEE J Quantum Electron 38 (2002), 1353–1365.
9. C. Monat, C. Seassal, X. Letartre, P. Regreny, M. Gendry, P. Rojo-Romeo, and P. Viktorovitch, Two-dimensional hexagonal-shaped microcavities formed in a two-dimensional photonic crystal on a InP membrane, J Appl Phys 93 (2003), 23–31.
10. D.S. Song, S.H. Kim, H.G. Park, C.K. Kim, and Y.H. Lee, Single-fundamental-mode photonic-crystal vertical-cavity surface-emitting lasers, Appl Phys Lett 80 (2002), 3901–3903.
11. H.T. Hattori, X. Letartre, C. Seassal, P. Rojo-Romeo, J.L. Leclercq, and P. Viktorovitch, Analysis of hybrid photonic crystal vertical cavity surface emitting lasers, Optics Express 11 (2003), 1799–1808.
12. D. Ohnishi, T. Okano, M. Imada, and S. Noda, Room temperature continuous wave operation of a surface-emitting two-dimensional photonic crystal diode laser, Optics Express 12 (2004), 1562–1568.
13. C. Monat, C. Seassal, X. Letartre, P. Viktorovitch, P. Regreny, M. Gendry, P. Rojo-Romeo, G. Hollinger, E. Jalaguier, S. Pocas, and B. Aspar, InP two-dimensional photonic crystal on silicon: In-plane Bloch mode laser, Appl Phys Lett 81 (2002), 5102–5104.
14. S.H. Kwon, H.Y. Ryu, G.H. Kim, and Y.H. Lee, Photonic bandedge lasers in two-dimensional square-lattice photonic crystal slab, Appl Phys Lett 83 (2002), 3870–3872.
15. J.S. Foresi, Photonic bandgap microcavities in channel waveguides, Nature 390 (1997), 143–145.
16. L. Florescu, K. Busch, and S. John, Semiclassical theory of lasing in photonic crystals, J Optics Soc Am B 19 (2002), 2215–2223.
17. J. Topol'ancik, S. Pradhan, P.-C. Yu, S. Gosh, and P. Bhattacharya, Electrically injected photonic crystal edge-emitting quantum-dot laser source, IEEE Photon Technol Lett 16 (2004), 960–962.
18. H.T. Hattori, V.M. Schneider, R.M. Cazo, C.L. Barbosa, Analysis of strategies to improve the directionality of photonic crystal band-edge structures, Appl Optics (to appear).

than 4%), h is the Planck's constant, q is the electronic charge, and η_d is the differential quantum efficiency. Figure 4(a) shows the power coupled to the waveguide as a function of the injection current. It is noted that we may expect that the power coupled into the waveguide is in the region of hundreds of μW for typical injection currents.

As the vertical losses depend upon the vertical structure of the slab (the materials chosen and geometrical parameters), we have analyzed the effect of P_{vert} on the threshold current and the differential quantum efficiency of this device. The threshold current as a function of P_{vert} is shown in Figure 4(b). The threshold current starts to become large for $P_{vert} > 0.5$, which means that for $P_{vert} > 0.5$, it will be hard for this device to "lase." The differential quantum efficiency as a function of P_{vert} is shown in Figure 4(c). As can be observed in this figure this efficiency also degrades sensibly for $P_{vert} > 0.5$ and its dependence with respect to P_{vert} is nearly hyperbolical.

19. S.G. Johnson and J. Joannopoulos, Bloch-iterative frequency domain methods for Maxwell's equations in a planewave basis, Opt Express 8 (2001), 173–190.
20. N. Susa, Threshold gain and gain-enhancement due to distributed-feedback in two-dimensional photonic crystal lasers, J Appl Phys 89 (2001), 815–823.
21. C. Wilsen, H. Temkin, and L.A. Coldren, Vertical-cavity surface-emitting lasers: Design, fabrication, characterization and applications, Cambridge University Press, Cambridge, UK, 2001.

HIGH-GAIN PRINTED DIPOLE ANTENNA

Yung-Tao Liu, Ting-Chih Tseng and Kin-Lu Wong
Department of Electrical Engineering
National Sun Yat-Sen University
Kaohsiung 804, Taiwan

ABSTRACT: *A printed dipole antenna showing high gain (about 6.8 dBi) radiation in the azimuthal plane is presented. The dipole antenna has a narrow width of 10 mm and a total length of about 202 mm (with 1.64 wavelengths of the frequency at 2442 MHz, the center frequency of the 2.4-GHz WLAN band). In each one of the two radiating arms of the dipole antenna, a meandered line is inserted as a phase-reversal device. With this arrangement, the proposed dipole antenna performs as a collinear array antenna with three in-phase half-wavelength radiating elements, leading to constructive radiation in the azimuthal plane and small side lobes in the elevation plane.* © 2005 Wiley Periodicals, Inc. Microwave Opt Technol Lett 46: 214–218, 2005; Published online in Wiley InterScience (www.interscience.wiley.com). DOI 10.1002/mop. 20948

1. INTRODUCTION

Conventional dipole antennas are usually constructed from coaxial lines and operated as a half-wavelength resonant structure [1]. This kind of coaxial dipole antenna usually shows an antenna gain of about 2.2 dBi only. However, for some practical applications such as in the access point for wireless local area networks (WLANs) [2], a much larger antenna gain may be required. To achieve a high-gain dipole antenna, one can use several half-wavelength coaxial-line sections, in which their inner and outer conductor connections are reversed at each junction, to form a coaxial collinear antenna with in-phase radiating sections in order to achieve an enhanced gain [3, 4]. A planar or printed type of this design with seven 50Ω microstrip-line sections has been recently demonstrated, and an antenna gain of about 5.0 dBi has been obtained [5]. Another promising method for obtaining a high-gain dipole antenna is to use a meandered-line section to act as a phase-reversal device [6–8] in the radiating arms of a long dipole or monopole antenna. This arrangement has a simpler configuration than the design in [3–5] and can also provide a collinear-array antenna structure with in-phase radiating elements, thus making possible an enhanced antenna gain for the dipole antenna.

Based on the use of a meandered-line section as the phase-reversal device [6–8], we propose in this paper a high-gain printed-dipole antenna suitable for replacing the conventional coaxial antennas for WLAN access-point applications. The proposed printed-dipole antenna has the advantage of low cost in fabrication, compared to coaxial antennas. Furthermore, the proposed antenna

can provide a high antenna gain of about 6.8 dBi for operation in the 2.4-GHz WLAN band (2400–2484 MHz). Design considerations of the proposed antenna are described, and results of the constructed prototype are presented and discussed.

2. DESIGN CONSIDERATIONS OF THE PROPOSED ANTENNA

Figure 1 shows the geometry of the proposed high-gain printed dipole antenna. Note that the dimensions given in the figure are for operating in the 2.4-GHz band. The antenna has two identical radiating arms printed on an inexpensive 0.4-mm-thick FR4 substrate and is fed at points A and B by a 50Ω mini coaxial line with a balun attached. Also note that in this design the antenna is designed to have a narrow width of 10 mm, which is comparable to that of conventional coaxial antennas. This narrow width makes the proposed antenna suitable for replacing the conventional coaxial antennas in practical applications.

The antenna can be divided into five sections: element 1, element 2, elements 3a and 3b, element 4, and element 5. These five sections (from elements 1 to 5) can be considered to correspond to the half-wavelength elements A to E of a conventional 2.5-wavelength dipole antenna, as shown in Figure 2. It can be seen that the currents in elements B and D have a phase opposite to those of elements A, C, and E. In this case, large destructive effects caused by the radiation contributed from the five elements
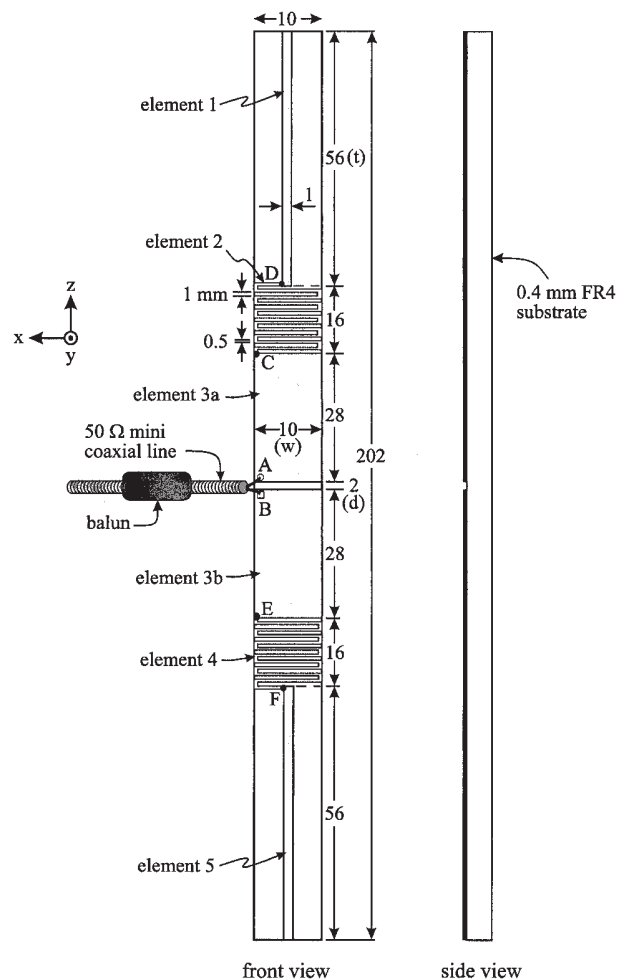

Figure 1 Geometry of the proposed high-gain printed dipole antenna